CrossMark

Effects of sintering temperature on the microstructure and thermoelectric properties of mesostructured $Co_4Sb_{11.5}Te_{0.5}$ skutterudites dispersed nano-TiN

Houjiang Yang[1] · Pengfei Wen[1] · Yan Zhu[2] · Bo Duan[1] · Xilong Zhou[1] · Pengcheng Zhai[1]

Abstract

The mesostructured skutterudites $Co_4Sb_{11.5}Te_{0.5}$ + nano-TiN composites are prepared through ball milling and spark plasma sintering (SPS). The influence of the various SPS temperatures within the range of 813–933 K on the microstructure and thermoelectric properties are focus in this work. The average grain sizes of the skutterudites increase from ~110 to ~500 nm with the increasing SPS temperature, while the densities of composites decrease from 7.02 to 6.26 g cm^{-3}. Additionally, the phase of $CoTe_2$ is detected in the samples sintered at 903–933 K. With the SPS temperature increasing from 813 to 903 K, the electrical conductivity and thermal conductivity increase simultaneously, and then decrease when SPS temperature rises to 933 K. The absolute value of Seebeck coefficient shows no clear changes when SPS temperature is not higher than 873 K but then slightly decreases with the increasing of SPS temperature. At last, the optimum SPS temperature is determined as 873 K, the *ZT* value of 1.07 at 800 K for the sample SPSed at 873 K is obtained, which is 11.5% higher than that of the sample SPSed at 903 K.

1 Introduction

Thermoelectric (TE) materials can directly convert heat into electricity (Seebeck effect) and vice-versa (Peltier effect). Hence they have drawn substantial attention due to their promising application in power generation and cooling [1–3]. The performance of a TE material is determined by its dimensionless figure of merit $ZT = \alpha^2\sigma T/\kappa$, where α is the Seebeck coefficient, σ is the electrical conductivity, T is the absolute temperature, and κ is the thermal conductivity.

$CoSb_3$-based skutterudites possess a great potential in power generation application in intermediate temperatures (600–900 K) due to their excellent power factor $\alpha^2\sigma$. But it displays a too large thermal conductivity that must be cut down to achieve high *ZT* values for practice applications

[4, 5]. Therefore, numerous efforts on $CoSb_3$-based skutterudites were concentrated on suppressing the thermal conductivity and thus improve the TE performance [6–9]. Thereinto, nanostructuring and introducing nano inclusion were regarded as two effective methods to suppress the thermal conductivity [10–12]. Recently, a strategy combining grain refinement and introducing nano inclusion was presented to further suppress the thermal conductivity based on the stronger grain boundary scattering of phonons [13]. However, some studies have reported that the grain sizes of refined particles are temperature sensitive. Normally, higher sintering temperature leads to larger grain size [14, 15]. Meanwhile, it was also reported that the higher sintering temperature will lead to the higher Sb-vacancy [16]. Additionally, it is noteworthy that the interactions between matrix and inclusion originated from the mismatch of thermal expansion coefficient of the two materials are inevitable and temperature related [17]. Thus it is very necessary to study the effect of sintering temperature on the structure and TE properties of the sample with refined particles and nano inclusions.

In the present work, the refined $Co_4Sb_{11.5}Te_{0.5}$ bulks dispersed nano TiN (20 nm, 1 vol%) are prepared through ball milling (BM) and spark plasma sintering (SPS). The influences of the SPS temperatures on the structure and the

✉ Pengfei Wen
    pfwen@126.com

[1] Hubei Key Laboratory of Theory and Application
    of Advanced Materials Mechanics, School of Science,
    Wuhan University of Technology, Wuhan 430070, Hubei,
    China

[2] School of Civil and Architectural Engineering, Wuhan
    Huaxia University of Technology, Wuhan 430223, Hubei,
    China

TE properties of the samples are investigated. Nano-TiN is chosen as the inclusion for its high temperature stability (melt point: 3223 K), excellent mechanical strength and has a similar thermal expansion coefficient (9.35×10^{-6} K^{-1}) [18] to that of skutterudites (8.66×10^{-6} K^{-1}) [19].

2 Experimental details

Commercial powders Co (99.9%), Sb (99.99%), and Te (99.9999%) were used as starting materials and weighted according to the stoichiometric ratio of $Co_4Sb_{11.5}Te_{0.5}$. The powders were mixed in an agate mortar, loaded into carbon crucibles and sealed in vacuum quartz tubes, then heated slowly to 903 K and held for 50 h. The obtained ingots were ground into powders, mixed with nano-TiN powders (1 vol%), then milled for 50 h at 300 rpm. The milled $Co_4Sb_{11.5}Te_{0.5}$/TiN composite powders were sintered by SPS under 40 MPa for 7 min at different temperatures from 813 to 933 K. The sintered bulks were named as S813, S843, S873, S903 and S933, respectively.

Phase purity was verified by using X-ray diffraction (XRD; Bruker: D8 Advance, Cu Ka). The morphology of powders and bulk samples were performed by field-emission scanning electron microscopy (FESEM; Zeiss Ultra plus, Germany). The back-scattered electron (BSE) images and element distributions of the polished surfaces were obtained with an electron probe micro analyzer (EPMA; JXA-8230, Japan). The electrical conductivity σ and Seebeck coefficient α were measured concurrently by the standard four-probe method under He atmosphere (ZEM-3; Sinku-riko, Japan). The Hall Coefficient R_H was measured at 300 K using a physical properties measurement system (PPMS, Quantum Design) in the magnetic field of ± 1 T. The carrier concentration n and Hall mobility μ_H were calculated by using the

relations $n = 1/(qR_H)$ and $\mu_H = \sigma R_H$, where q is the carrier charge. The thermal conductivity κ was calculated from the measured thermal diffusivity λ, heat capacity C_p, and density d by the relationship of $\kappa = C_p\lambda d$. Cp and λ were measured by the differential scanning calorimeter (TA: DSC Q20) and a laser-flash technique (Netzsch: LFA457), and d was measured with the Archimedes method. Uncertainties in σ and κ are ± 5–7%. The uncertainty in α is ± 5%.

3 Results and discussion

Figure 1a shows the XRD patterns of the $Co_4Sb_{11.5}Te_{0.5}$ powders before BM and the $Co_4Sb_{11.5}Te_{0.5}$/TiN composite powders after BM. As can be seen, all of the diffraction peaks are indexed in the single skutterudite phase. No trace of TiN phase is detected in $Co_4Sb_{11.5}Te_{0.5}$/TiN composite powders because of the low volume content. In addition, it is obvious that the XRD pattern of the milled $Co_4Sb_{11.5}Te_{0.5}$/TiN composite powders shows broader and weaker diffraction peaks as compared with that of the $Co_4Sb_{11.5}Te_{0.5}$ powders before BM, which is owing to the size effect and considerable amount of strains in nanopowders [20]. The milled powders exhibit an average grain size of 40 nm approximately, as calculated by the Scherrer's formula [21],

$$l = k\lambda/(\beta cos\theta)$$

where l is the grain size, k is a constant, λ is the X-ray wavelength, β is the peak widening of full width at half maximum and θ is the diffraction angle, respectively.

Figure 1b shows the XRD patterns of bulk $Co_4Sb_{11.5}Te_{0.5}$/TiN composites sintered at different temperatures. As can be seen, when the SPS temperatures range from 813 to 873 K, the samples are composed of a single phase with the skutterudite structure, but the phase of $CoTe_2$ is detected in the
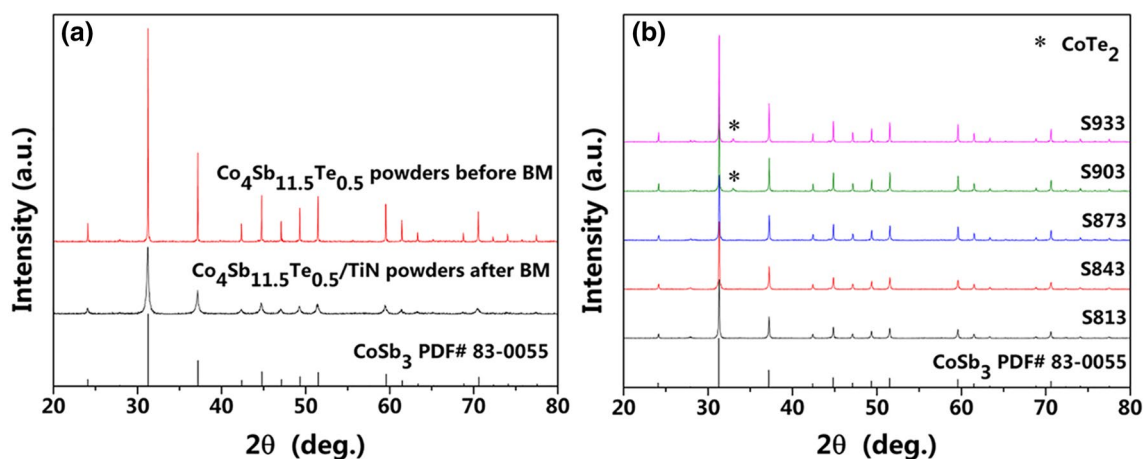

Fig. 1 a XRD patterns of the powders of $Co_4Sb_{11.5}Te_{0.5}$ before BM and $Co_4Sb_{11.5}Te_{0.5}$/TiN after BM, **b** XRD patterns of the samples sintered at different temperatures. (Color figure online)

samples sintered at 903–933 K. The phase of $CoTe_2$ also has been found in the $Co_4Sb_{11.5}Te_{0.5}$ consolidated by hot press at 898 K in the literature [22]. In addition, the densities of the samples sintered different temperatures are listed in Table 1. It is worth noting that the densities of the samples decrease with the increasing SPS temperature, which is inconsistent with some other literatures [23, 24]. The decline in density is maybe due to the following two reasons. Firstly, Sb volatilization is inevitable and increasing as the sintering temperature increases, resulting in a decrease in the mass of samples with the increase of the sintering temperature [16]. Secondly, the interaction between $Co_4Sb_{11.5}Te_{0.5}$ and the TiN particles during sintering stage, deriving from the mismatch of the thermal expansion coefficient between these two materials [17], will become stronger and stronger with the increasing sintering temperature, leading to an expanding of volume.

Figure 2 displays the elemental distributions and the BSE image of the sample S873. The EDX elemental distribution results indicate that Co, Sb, Te, Ti and N in the S873 are distributed homogeneously. The BSE contrast is consistent with no traces of any impurity phase, which is in accordance with the result of XRD pattern shown in Fig. 1b.

Figure 3a shows the FESEM image of the milled $Co_4Sb_{11.5}Te_{0.5}/TiN$ composite powders. It evidences that the powders are composed of the nanocrystal with grain size

approximately 20–80 nm in diameter, which is accordance with the result calculated by the Scherrer's formula. Figure 3b–f show the FESEM images of fracture surfaces of bulks sintered at different temperatures. As can be seen, it is clear that the grain sizes of the sintered samples become larger compared with that of the ball milled powders. Furthermore, with the SPS temperature increasing from 813 to 933 K, the grain grows increasingly large, which is consistent with the results of other literatures [15, 23]. The average grain size of the samples is listed in Table 1.

Figure 4a displays the temperature dependence of electrical conductivity for the samples sintered at different temperatures. As can be seen, all samples display a decreasing electrical conductivity with the increasing temperature, showing a characteristic of degenerate semiconductors. For the samples sintered at the temperature from 813 to 903 K, the electrical conductivity increases with the increasing SPS temperatures, which is mainly due to the increasing carrier concentration and carrier mobility, as presented in Table 1. Here, the increase in carrier concentration is induced by the growing number of Sb-vacancy with increasing SPS temperature [16], and the increase in carrier mobility is due to the growth of grain size decreasing the boundary scattering of carriers [25]. However, it is found that the electrical conductivity of S933 is lower than that of S903. It is mainly attributed to the lower carrier mobility induced by the higher

Table 1 Some room-temperature properties of samples sintered at different temperatures

Sample	Density (g cm^{-3})	Porosity (%)	R_H (10^{-2} cm^3 C^{-1})	n (10^{20} cm^{-3})	μ_H (cm^2 V^{-1} s^{-1})	Average grain size (nm)
S813	7.02	8	−1.88	3.32	12.39	~110
S843	6.86	10	−1.84	3.40	12.67	~150
S873	6.54	15	−1.72	3.63	13.45	~270
S903	6.45	16	−1.69	3.70	13.80	~350
S933	6.26	18	−1.68	3.72	12.94	~500

Fig. 2 EDX elemental distribution maps and the BSE image of the sample sintered at 873 K. (Color figure online)
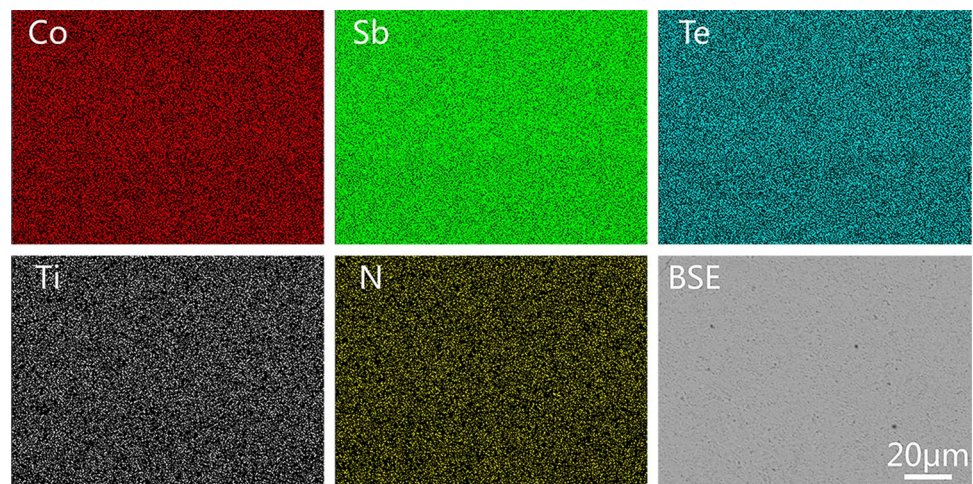
Fig. 3 FESEM image of **a** milled $Co_4Sb_{11.5}Te_{0.5}$/TiN composite powders and **b**–**f** fracture surfaces of the bulks sintered at different temperatures
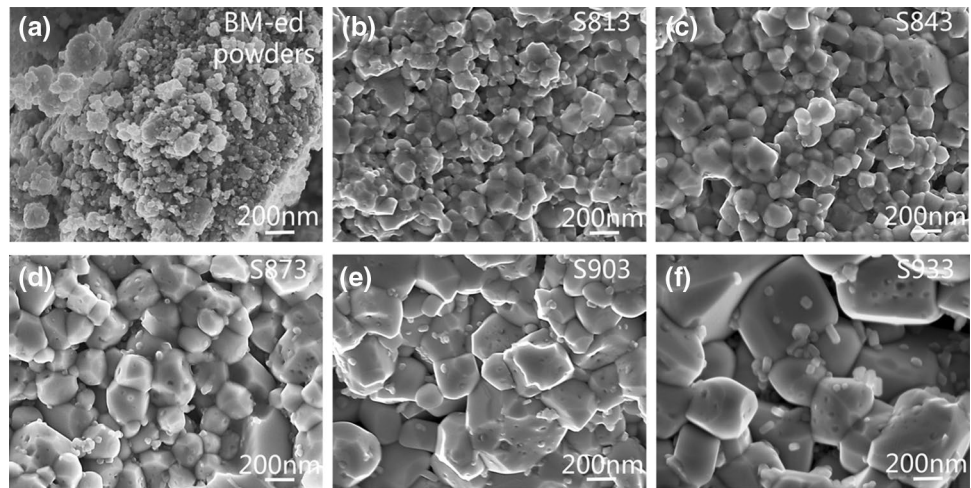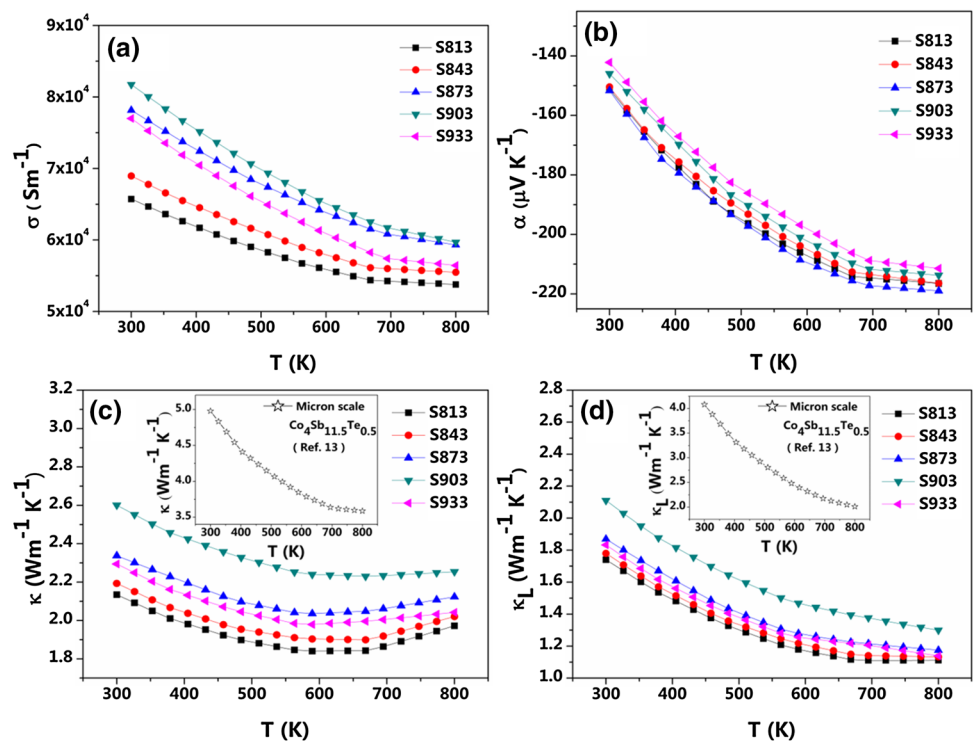

Fig. 4 Temperature dependence of **a** electrical conductivity, **b** Seebeck coefficient, **c** thermal conductivity, **d** lattice thermal conductivity for the samples sintered at different temperatures. (Color figure online)

porosity and Sb-vacancy. Assume the sample is composed of particles and pores, the reduction in σ may be triggered by the formula [26]

$$\sigma = \frac{(3C-1)}{2}\sigma_f$$

where C and σ_f are the relative density and the theoretic electrical conductivity, respectively. If we consider 2% decrease in relative density for S933 compare with S903. The estimated plunge in electrical conductivity should be around 4% by using this formula, but it actually declines 6%. Thus, the scattering of the carriers induced by the

Sb-vacancy may be another reason for the decrease of electrical conductivity of S933.

Figure 4b shows the temperature dependence of Seebeck coefficient for all samples sintered at different SPS temperatures. As can be seen, all the samples show n-type conduction with negative Seebeck coefficient. The absolute values of Seebeck coefficient at 300 K change little when SPS temperatures are not higher than 873 K, but then slightly decrease with the increase of SPS temperature. The decrease of the $|\alpha|$ may mainly attribute to the slightly increased carrier concentration and the metallic $CoTe_2$ secondary phase [27].

Figure 4c shows the temperature dependence of thermal conductivity κ for the samples sintered at different temperatures. As can be seen, the κ of all samples shows evidence of rise at high temperature (above 600 K), indicating intrinsic excitations (bipolar effect) [28]. Additionally, the κ increases with the increase of SPS temperature from 813 to 903 K, while it decreases when the SPS temperature rises at 933 K. To eliminate the effect of the electronic thermal conductivity, the lattice thermal conductivity κ_L is obtained by subtracting the electronic part κ_E from the total thermal conductivity using the Wiedemann–Franz law ($\kappa_E = L\sigma T$) with the Lorenz number L of 2×10^{-8} V^2 K^{-2} [29]. The lattice thermal conductivity κ_L of the samples is shown in Fig. 4d. It can be seen that the main contribution to κ is primarily from the κ_L. The lowest lattice thermal conductivity of 1.74 Wm^{-1} K^{-1} at 300 K is obtained for the sample S813, but the value of the lattice thermal conductivity at 300 K increases to 2.11 Wm^{-1} K^{-1} when the SPS temperature increases at 933 K. This is largely owing to the decreasing phonon scattering by enhancing grain sizes [30]. However, the lattice thermal conductivity of the S933 decreases as compared with that of the S903, which may be partly attributed to the bigger porosity. According to the effective medium theory [25, 31], the relationship between porosity and lattice thermal conductivity is used to be described by the equation

$$\kappa = \kappa_0 \frac{2 - 2p}{2 + p}$$

where κ_0, p, are the theoretical lattice thermal conductivity and the porosity, respectively. If we consider 2% increase in porosity for S933 compare with S903. The estimated plunge in lattice thermal conductivity should be around 4% by using this equation, but the 13% drop in lattice thermal conductivity of S933 than that of S903. Thus, the scattering of phonons due to the amounts of Sb-vacancy may be another reasons for the decline of thermal conductivity [32].

Figure 5 shows the temperature dependence of the dimensionless figure of merit ZT for the samples sintered at different temperatures. As can be seen, the effect of SPS temperature on the ZT value is evident. For the S903, the ZT at 800 K is 0.96. But, the ZT value is 1.07 at 800 K for the sample S873, a difference of about 11.5%.

4 Conclusion

The SPS temperature has obvious effect on the structure and TE properties of the mesostructured skutterudites $Co_4Sb_{11.5}Te_{0.5}$ + nano-TiN composites. The samples sintered at 813–873 K are composed of a single phase compound with the skutterudite structure, but a trace of $CoTe_2$
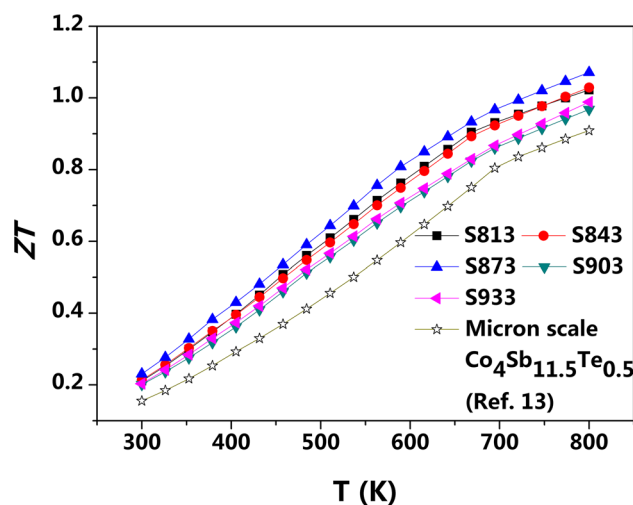

Fig. 5 Temperature dependence of dimensionless figure of merit ZT for the samples sintered at different temperatures. (Color figure online)

is detected in the samples sintered at 903–933 K. The average grain sizes grow increasingly large from 110 to 500 nm when the SPS temperature increases from 813 to 933 K. The density decreases with the increase of SPS temperature. With the SPS temperature increasing from 813 to 903 K, the electrical conductivity and thermal conductivity increase simultaneously, and then decrease when SPS temperature rises to 933 K. The absolute value of Seebeck coefficient shows no clear changes when SPS temperature is not higher than 873 K but then slightly decreases with the increasing of SPS temperature. The maximum ZT value of 1.07 is obtained at 800 K for the sample sintered at 873 K, but that of the sample sintered at 903 K is only 0.96, a difference of about 11.5%.

References

1. L.E. Bell, Science **321**, 1457–1461 (2008)
2. G.J. Snyder, E.S. Toberer, Nat. Mater. **7**, 105–114 (2008)
3. M.R. Bravo, A. Moure, J.F. Fernández, M.M. González, RSC Adv. **5**, 41653–41667 (2015)
4. H. Anno, K. Matsubara, Y. Notohara, T. Sakakibara, H. Tashiro, J. Appl. Phys. **86**, 3780–3786 (1999)
5. E. Alleno, E. Zehani, M. Gaborit, V. Orodniichuk, B. Lenoir, M. Benyahia, J. Alloy. Compd. **692**, 676–686 (2017)
6. T. Dahal, Q. Jie, G. Joshi, S. Chen, C.F. Guo, Y.C. Lan, Z.F. Ren, Acta. Mater. **75**, 316–321 (2014)

7. L. Deng, H.A. Ma, T.C. Su, F.R. Yu, Y.J. Tian, Y.P. Jiang, N. Dong, S.Z. Zheng, X. Jia, Mater. Lett. **63**, 2139–2141 (2009)

8. M.S. Toprak, C. Stiewe, D. Platzek, S. Williams, L. Bertini, E. Müller, C. Gatti, Y. Zhang, M. Rowe, M. Muhammed, Adv. Funct. Mater. **14**, 1189–1196 (2004)

9. X.Y. Zhou, G.Y. Wang, L. Zhang, H. Chi, X.L. Su, J. Sakamoto, C. Uher, J. Mater. Chem. **22**, 2958–2964 (2012)

10. J.L. Mi, T.J. Zhu, X.B. Zhao, J. Ma, J. Appl. Phys. **101**, 054314 (2007)

11. H. Li, X.F. Tang, X.L. Su, Q.J. Zhang, C. Uher, J. Phys. D **42**, 145409 (2009)

12. B. Feng, J. Xie, G.S. Cao, T.J. Zhu, X.B. Zhao, J. Mater. Chem. A **1**, 13111 (2013)

13. P.F. Wen, H.J. Yang, X.L. Zhou, B. Duan, P.C. Zhai, Mater. Lett. **223**, 190–193 (2018)

14. S. Bathula, M. Jayasimhadri, B. Gahtori, N.K. Singh, K. Tyagi, A.K. Srivastava, A. Dhar, Nanoscale **7**, 12474–12483 (2015)

15. A. Khan, M. Saleemi, M. Johnsson, L. Han, N.V. Nong, M. Muhammed, M.S. Toprak, J. Alloy. Compd. **612**, 293–300 (2014)

16. W.S. Liu, B.P. Zhang, J.F. Li, L.D. Zhao, J. Phys. D **40**, 566–572 (2007)

17. P.F. Wen, B. Duan, P.C. Zhai, P. Li, Q.J. Zhang, J. Mater. Sci-Mater. El. **24**, 5155–5161 (2013)

18. D.S. Stone, K.B. Yoder, W.D. Sproul, J. Vac. Sci. Technol. A **9**, 2543–2547 (1991)

19. G. Rogl, P. Rogl, Sci. Adv. Mater. **3**, 517–538 (2011)

20. A. Usenko, D. Moskovskikh, A. Korotitskiy, M. Gorshenkov, E. Zakharova, A. Fedorov, Y. Parkhomenko, V. Khovaylo, Scripta Mater. **146**, 295–299 (2018)

21. P. Scherrer, Math. Phys. Klasse. **2**, 98–100 (1918)

22. Z. Qin, K.F. Cai, S. Chen, Y. Du, J. Mater. Sci-Mater. El. **24**, 4142–4147 (2013)

23. J. Pei, B.P. Zhang, J.F. Li, D.D. Liang, J. Alloy. Compd. **728**, 694–700 (2017)

24. S.S. Lim, J.H. Kim, B. Kwon, S.K. Kim, H.H. Park, K.S. Lee, J.M. Baik, W.J. Choi, D.I. Kim, D.B. Hyun, J.S. Kim, S.H. Baek, J. Alloy. Compd. **678**, 396–402 (2016)

25. C.C. Zhang, X.A. Fan, J. Hu, C.P. Jiang, B. Feng, Q.S. Xiang, G.Q. Li, Y.W. Li, Adv. Eng. Mater. **18**, 1777–1784 (2016)

26. R. Landauer, J. Appl. Phys. **23**, 779–784 (1952)

27. A.U. Khan, K. Kobayashi, D.M. Tang, Y. Yamauchi, K. Hasegawa, M. Mitome, Y.M. Xue, B.Z. Jiang, K. Tsuchiya, D. Golberg, Y. Bando, T. Mori, Nano Energy **31**, 152–159 (2017)

28. W.Y. Zhao, P. Wei, Q.J. Zhang, W.T. Zhu, X.L. Su, X.F. Tang, J.H. Yang, Y. Liu, J. Shi, Y.M. Chao, S.Q. Lin, Y.Z. Pei, Nat. Nanotechnol. **12**, 55–60 (2017)

29. B.C. Sales, B.C. Chakoumakos, V. Keppens, J.R. Thompson, Phys. Rev. B **56**, 15081–15089 (1997)

30. C.W. Nan, R. Birringer, Phys. Rev. B **57**, 8264–8268 (1998)

31. M. Takashiri, S. Tanaka, H. Hagino, K. Miyazaki, J. Appl. Phys. **112**, 084315 (2012)

32. P.F. Wen, P. Li, Q.J. Zhang, F.J. Yi, L.S. Liu, P.C. Zhai, J. Electron. Mater. **38**, 1200–1205 (2009)